Check for updates

physica status solidi rrl

www.pss-rapid.com

Understanding Reproducibility of Sputter-Deposited Metastable Ferroelectric Wurtzite $Al_{0.6}Sc_{0.4}N$ Films Using In Situ Optical Emission Spectrometry

Daniel Drury, Keisuke Yazawa, Allison Mis, Kevin Talley, Andriy Zakutayev, and Geoff L. Brennecka**

High-Sc $Al_{1-x}Sc_xN$ thin films are of tremendous interest because of their attractive piezoelectric and ferroelectric properties, but overall film quality and reproducibility are widely reported to suffer as x increases. In this study, structural and electrical properties of metastable $Al_{0.6}Sc_{0.4}N$ films are connected with plasma changes during film growth, identified via glow discharge optical emission spectroscopy (GD-OES), and linked to the target mode changes. This in situ GD-OES technique uses changes in the N_2(I) intensity, correlated with DC bias hysteresis behavior of a $Al_{0.6}Sc_{0.4}$ target in metallic and poisoned modes, to identify films that subsequently exhibit unacceptable structural and electrical performance. Two representative samples deposited under identical conditions but possessing distinct properties related to phases present in the films are focused on. Films sputtered under a poisoned target mode produce pure wurtzite ferroelectric $Al_{0.6}Sc_{0.4}N$ with a reversible 80 μC cm^{-1} polarization and 3.1 MV cm^{-1} coercive field. When identical chamber settings are used but the process starts in metallic mode, a mixed wurtzite/rocksalt film is deposited which exhibits nanometer-scale changes to the film microstructure and a nonferroelectric response. These results illustrate the utility of optical emission spectroscopy for tracking target mode fluctuations when fabricating metastable materials such as high-Sc $Al_{1-x}Sc_xN$ films.

1. Introduction

Interest in the growth of AlN-based group III metal nitride semiconductor alloys such as (Al,Ga)N and (Al,In,Ga)N continues to increase as the associated application space expands. First, the interest was driven by their tunable properties for light-emitting diodes (LEDs) and other optoelectronic applications [1] and by their wide bandgap (WBG) semiconductor properties for high electron mobility transistors (HEMTs) in radio frequency (RF) and power electronic applications.[2] Scandium additions to AlN were first reported to produce significant increases in piezoelectric response in 2009[3] and were very quickly adopted for the piezoelectric thin film devices such as film bulk acoustic resonators (FBARs) in cell phones.[4] Recent reports on ferroelectricity in $Al_{1-x}Sc_xN$ for $x \geq 0.1$ have sparked additional scientific interest as the first wurtzite ferroelectric material[5,6] and significant technological interest as a candidate for hybrid logic-in-memory devices.

Large-scale commercial applications of piezoelectric $Al_{1-x}Sc_xN$ are still limited to relatively modest levels of Sc substitution ($x < 0.1$), though there are many literature reports of $Al_{1-x}Sc_xN$ films having $x \geq 0.1$ with exceptional properties.[3–12] It has been widely reported that increasing Sc content, desired for increased piezoelectric response and lower field ferroelectric switching, increases the challenge of growing high-quality textured $Al_{1-x}Sc_xN$ films.[13–15] This challenge is driven in no small part by the thermodynamic driving force for phase separation in this highly metastable material system.[16,17] This degradation in film properties for large x values has been correlated with wurtzite-(0002) texture reduction with the presence of misoriented grains[11] and the associated difficulties with reliably controlling the stress state in sputtered films.[18] However, in each case the conclusions are correlational and are drawn largely or entirely from ex situ measurements, so they are of limited value for deposition process control.

Many in situ monitoring techniques have been reported for tuning the deposition of AlN thin films: glow discharge optical emission spectrometry (GD-OES),[19,20] reflection high-energy electron diffraction (RHEED),[21,22] reflectance interferometry

D. Drury, Dr. K. Yazawa, A. Mis, Dr. K. Talley, Dr. A. Zakutayev, Dr. G. L. Brennecka
Materials Science Center
National Renewable Energy Laboratory
Golden, CO 80401, USA

D. Drury, Dr. K. Yazawa, A. Mis, Dr. G. L. Brennecka
Department of Metallurgical and Materials Engineering
Colorado School of Mines
Golden, CO 80401, USA
E-mail: ddrury@mines.edu; geoff.brennecka@mines.edu

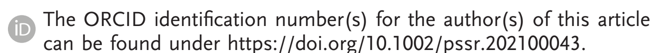
The ORCID identification number(s) for the author(s) of this article can be found under https://doi.org/10.1002/pssr.202100043.

© 2021 The Authors. physica status solidi (RRL) Rapid Research Letters published by Wiley-VCH GmbH. This is an open access article under the terms of the Creative Commons Attribution-NonCommercial License, which permits use, distribution and reproduction in any medium, provided the original work is properly cited and is not used for commercial purposes.

DOI: 10.1002/pssr.202100043

(RI),[23] and ellipsometry.[24] While useful as surface diagnostic tools for understanding how the film develops, RHEED, RI, and ellipsometry are costly methods which require significant adaptation to the system such as beam alignment. On the contrary, GD-OES only requires line of sight to the glow discharge. GD-OES is also able to evaluate the target poison mode for reactive depositions, which is an important step for optimizing RF sputtered nitrides.[20] However, there presently lacks literature on incorporating GD-OES when growing metastable $Al_{1-x}Sc_xN$, which is an opportunity considering the difficulty of producing a purely wurtzite phase, particularly for large values of x.

In this article, we investigate the process of sputtering metastable $Al_{1-x}Sc_xN$ thin films using GD-OES which is a well-known, nonintrusive, in situ monitoring technique. Consistent with the increased variability of film quality previously reported, metastable $Al_{0.6}Sc_{0.4}N$ films deposited in this study under identical settings for preconditioning steps and growth parameters exhibit drastically different structures and electrical properties. We clearly correlate changes in phase content and microstructure with deposition process fluctuations observed by time-resolved GD-OES. These process fluctuations are associated with changes in the target mode (metallic or poisoned) and have critical effects on resulting structural and electrical properties. For example, single-phase homogeneous $Al_{0.6}Sc_{0.4}N$ films deposited in a poisoned target mode exhibit clear ferroelectric switching. In contrast, $Al_{0.6}Sc_{0.4}N$ films grown using otherwise identical conditions but in a metallic target mode were two phase and showed no indication of ferroelectric polarization reversal. These results suggest that tracking target mode fluctuations, either by in situ GD-OES or by monitoring DC target bias, is important when fabricating highly metastable high-Sc $Al_{1-x}Sc_xN$ thin film materials.

2. Results

Figure 1a shows the X-ray diffraction (XRD) θ–2θ patterns for two representative films grown using the same deposition conditions and pretreatments that have previously been optimized for this chamber (see Experimental Section). The patterns indicate that one film has a pure c-axis textured wurtzite structure (wz-AlScN) and the other is a mixed wurtzite/rocksalt structure (wz/rs-AlScN). The wz-(0002) peak appears at 36.3° and corresponds to a c-axis lattice parameter of 0.494 nm for each sample which closely matches previous reports for $Al_{0.6}Sc_{0.4}N$.[11] The slight shoulder toward lower 2θ for wz-AlScN is related to a transition from initially in-plane compressive strain to tensile strain as the film grows.[6] In addition, there is a significant phase difference as indicated by the appearance of the (111) rocksalt peak at 35.7° as previously reported[3,25] and in line with theoretical work on the thermodynamic relationship between wurtzite and rocksalt in $Al_{1-x}Sc_xN$.[17] For samples grown using the same deposition conditions, it is interesting that there is a large discrepancy in phases. For both samples, the wz-(10-10) peak appears at 31.5° in Figure 1a. Figure 1b shows the wz-(0002) peak profile in χ space. This provides a similar film structure property as an ω-rocking curve which measures the out-of-plane texture of a particular 2θ position. 2D XRD patterns for each sample are provided in Figure S1, Supporting Information. In Figure 1b, we see similar out-of-plane texture between the two films, albeit a slightly lower full-width at half-maximum (FWHM) for wz-AlScN at 2.8° than the wz/rs-AlScN sample with 3.1°. Based on the broad χ FWHM (>10°), the (10-10) peak has poor out-of-plane texture.

Bright-field scanning transmission electron microscopy (BF-STEM) images in **Figure 2** revealed a columnar structure in both films with thicknesses of 325 and 337 nm for wz-AlScN and wz/rs-AlScN, respectively. The wz-AlScN sample exhibits a uniform structure through the thickness of the film, whereas striations are apparent in the wz/rs-AlScN sample as indicated by the timestamps. Assuming an overall constant deposition rate, the features occur at minutes 44, 56, 59, and 74 of the 110 min deposition. The selected-area electron diffraction (SAED) pattern of the wz/rs-AlScN film bulk in Figure 2c reveals that the film grows along the wz-[0001] and rs-[111] directions.

From the high-resolution TEM (HR-TEM) images of the wz/rs-AlScN sample provided in Figure S2, Supporting Information, selected areas were processed with a fast Fourier transform (FFT) to calculate the out-of-plane lattice spacings. The resulting spacings measured from the FFT of the bottom (2.50 Å) and top (2.46 Å) areas of the film closely match the

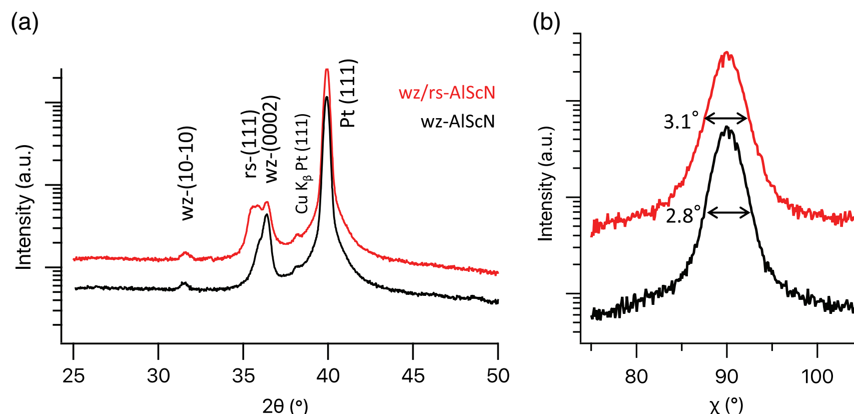

Figure 1. a,b) 1D XRD patterns of wz-$Al_{0.6}Sc_{0.4}$ N and wz/rs-$Al_{0.6}Sc_{0.4}$ N on platinized silicon substrates integrated from 2D XRD detector: a) 2θ patterns between 25° and 50° and b) χ pattern between 75° and 105° with associated FWHM.

© 2021 The Authors. physica status solidi (RRL) Rapid Research Letters published by Wiley-VCH GmbH

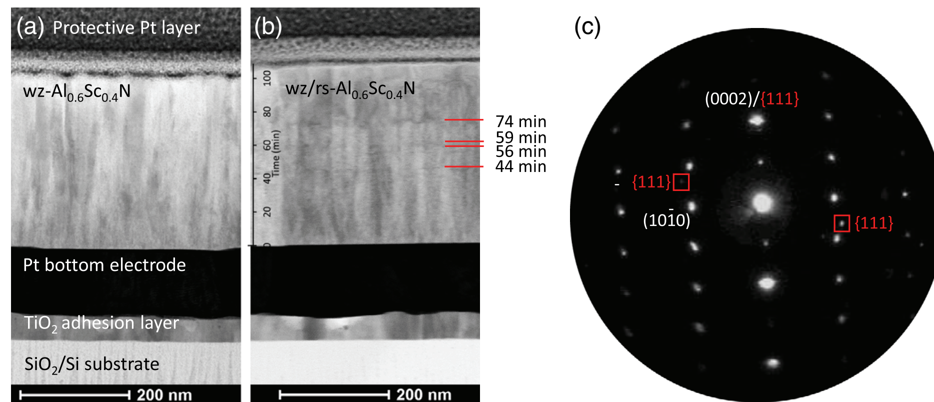

Figure 2. a) Bright-field STEM images of wz-$Al_{0.6}Sc_{0.4}N$ show a uniform microstructure in the cross section, while b) the wz/rs-$Al_{0.6}Sc_{0.4}N$ exhibits striations as marked by the timestamps. c) Resultant SAED pattern for wz/rs-AlScN showing out-of-plane wz-(0002) and rs-(111) film texture.

calculated spacings from the XRD patterns for the rs-(111) (2.52 Å) and wz-(0002) (2.47 Å) peaks, respectively. STEM–energy-dispersive X-ray spectroscopy (EDS) maps and profiles show no indication of chemical segregation in either sample (Figure S3, Supporting Information).

Optical emission of the glow discharge near the substrate surface was collected for all growths. The line at 337 nm which corresponds to an excited molecular N_2(I) state was tracked during the deposition (**Figure 3**). A representative full emission spectrum is provided in Figure S4, Supporting Information. There are four peaks the N_2 line for the wz/rs-AlScN sample that occur at times 44, 55, 59, and 71 min in Figure 3b. These peaks align in time with microstructural features in Figure 2b. However, the nearly uniform nature of the emission lines for wz-AlScN points toward a stable deposition in Figure 3b which led to a single phase and pure (0002) textured film in Figure 3a. No corresponding fluctuations in the in situ residual gas analyzer (RGA) signal were observed (Figure S5, Supporting Information).

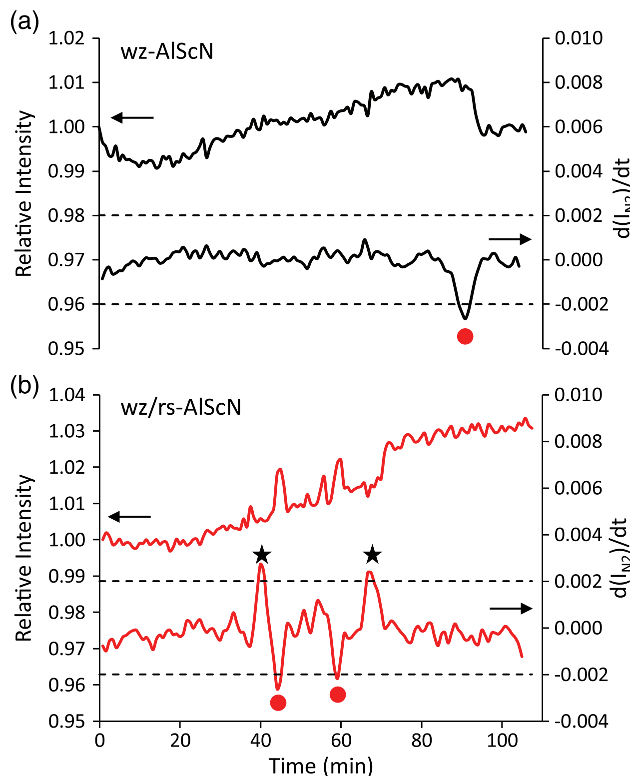

Figure 3. In situ data collected by OES. Relative intensity and dI/dt of N_2(I) for wz-AlScN (black) (a) and wz/rs-AlScN (red) (b) samples. The red circles indicate a transition from a poisoned to a metallic sputtering mode, the black stars correspond to changes from metallic to poisoned mode, and the dashed lines reflect the threshold used to mark when a transition occurs.

Polarization–electric field (P–E) hysteresis loops were measured on parallel plate capacitors fabricated from both thin film samples. In **Figure 4**a, the wz-AlScN P–E loop shows a saturated hysteresis loop indicative of the highly c-axis textured structure of the film. With a remanent polarization of 80 μC cm^{-1} and a coercive field of 3.1 MV cm^{-1}, the properties of this sample are consistent with previous reports on $x = 0.4$ chemistries in $Al_{1-x}Sc_xN$.[5,6] There is an ≈7% uncertainty associated with the polarization values due to uncertainty of the device area. In comparison, the mixed-phase layered wz/rs-AlScN sample did not exhibit ferroelectric switching up to 4.1 MV cm^{-1}; the maximum electric field sustained before catastrophic device failure. This result is consistent with the presence of a lower permittivity, nonferroelectric rocksalt phase in series with the ferroelectric wurtzite such that catastrophic macroscopic dielectric breakdown occurred before the portion of the field across the ferroelectric phase was sufficient to reverse polarization. The unsaturated P–E loops for wz/rs-AlScN in Figure 4a and apparent remanent polarization in Figure 4b are an effect of leakage currents during the voltage sweep and do not represent true ferroelectric behavior. Thus, the lack of ferroelectric properties in wz/rs-AlScN is due to series-connected rocksalt and wurtzite phases which are correlated with changes in target mode tracked by GD-OES during film growth.

3. Discussion

A variation in the intensity of the GD-OES lines in Figure 3 is linked to alterations of the target mode during sputtering which was determined by sweeping the ratio of $f = N_2/(N_2 + Ar)$ gas

© 2021 The Authors. physica status solidi (RRL) Rapid Research Letters published by Wiley-VCH GmbH

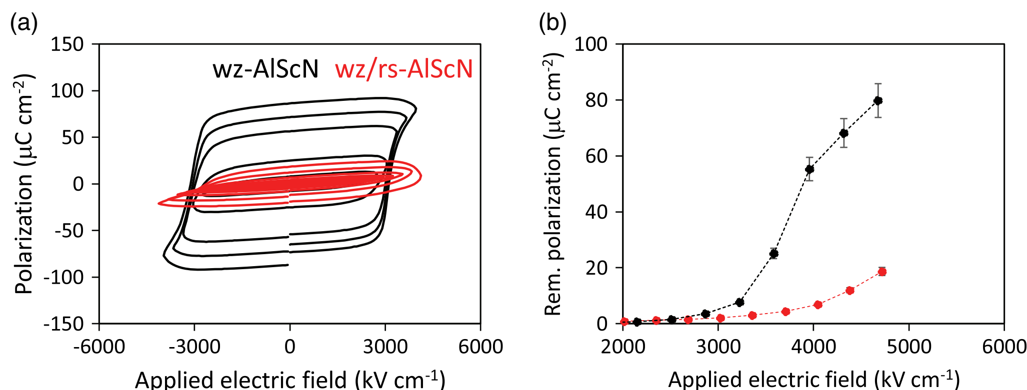

Figure 4. a) *P–E* loop hysteresis measurements of wz-$Al_{0.6}Sc_{0.4}N$ (black) and wz/rs-$Al_{0.6}Sc_{0.4}N$ (red) using a 10 kHz excitation frequency. b) Remanent polarization for both samples.

flow during sputtering and monitoring both the DC bias and the intensity of N_2(I) (Figure S6, Supporting Information). The change from metallic to poisoned regime occurs close to $f = 0.2$. As the deposition conditions reported in this article are located at $f = 0.25$, the sputtering target is in a sensitive state, close to the boundary between metallic and poisoned regimes of the AlSc alloy target. Figure S6b, Supporting Information, shows hysteretic behavior in the DC bias for $0 < f < 0.25$ which we associate with shifts between metallic and poisoned target modes. In support of this, Figure S6a, Supporting Information, reveals that the N_2(I) line intensity is highly dependent on the N_2 fraction for $0 < f < 0.3$. The peak at $f = 0.4$ for the N_2(I) intensity is due to the relative electron cross-section for the gaseous species in which N_2 > Ar for an electron energy of 20 eV. Rather than sputtering in a pure N_2 atmosphere, a N_2/Ar gas mixture is used to increase the density of excited N_2(I) species and, therefore, the energy of the reactive deposition.[26]

To track the active target mode during film deposition, the derivative of the N_2(I) line intensity with respect to time (dI/dt) is shown in Figure 3. By setting a threshold of $>|0.002|$, the shifts between different modes can be identified. For wz-AlScN (Figure 3a), it is apparent that the target sputters initially in a poisoned mode until minute 90 close to the end of a deposition where it transitions to a metallic mode. The wurtzite phase nucleates first and grows in the wz-[0001] direction, and the switch to metallic mode has a low impact as the rocksalt phase is undetected by XRD in Figure 1a. For wz/rs-AlScN mixed phase films (Figure 3b), the target is operating initially in a metallic mode and rocksalt nucleates and grows in the rs-[111] as observed in XRD peaks in Figure 1a and the HR-TEM in Figure S2a,c, Supporting Information. Then, once the target switches to a poisoned state at minute 44 leading to wurtzite nucleation, and once the wurtzite grains are fully established at minute 74, continued wurtzite growth occurs with wz-(0002) texture.

To summarize observations for wz-AlScN in Figure 3a and for wz/rs-AlScN in Figure 3b, it appears that when the target state changes from poisoned to metallic modes, the wurtzite growth on wurtzite is energetically favorable compared with rocksalt nucleation on wurtzite. This is not surprising because AlN strongly prefers growth as a [0001]-textured wurtzite, though it is commonly observed that the first few nm of films are untextured before the favored growth of the [0001] grains begins to dominate.[27] In contrast, ScN is stable in a rocksalt structure. So, if the target is initially in the metallic state, rocksalt nucleation is preferred, and rocksalt growth from rocksalt nuclei occurs. However, once the target switches to poisoned mode, wurtzite nucleation occurs and continues until completion of growth. The distinction between enhanced nucleation of wurtzite on rocksalt and suppressed nucleation of rocksalt on wurtzite is likely related to difference in relative mixing enthalpies of these two structures at $x = 0.40$ composition in a metastable $Al_{1-x}Sc_xN$ alloy. A two-phase wurtzite–rocksalt mixture is the thermodynamic ground state for this heterostructural alloy, but the mixing enthalpy in WZ structure (350–400 meV fu^{-1}) is smaller than in the RS structure (500–550 meV fu^{-1}).[17]

4. Conclusions

Metastable $Al_{0.6}Sc_{0.4}N$ film deposition process changes observed by in situ time-resolved GD-OES influence the overall phase purity, microstructure, and properties of the samples, and can be linked to fluctuations in the target mode for an $Al_{0.6}Sc_{0.4}$ alloy target. Performing reactive RF sputtering close to the boundary between metallic and poisoned modes is important because it maximizes deposition rate, N_2 chemical potential, and helps quenching in chemical homogeneity despite severe thermodynamic metastability. However, such metastable material synthesis requires constant monitoring of the deposition process, by GD-OES and/or by monitoring the target DC bias. Particularly early in film growth, a metallic target mode can promote the growth of an undesired rocksalt phase, whereas a poisoned target mode promotes the growth of the wz-$Al_{0.6}Sc_{0.4}N$. These changes apparent in the XRD, SAED, and BF-STEM measurements directly connect phase segregation into rocksalt and wurtzite with changes in GD-OES signal which is linked to changes in the target mode. The in situ GD-OES technique also allows for monitoring subsequent film properties because the peaks in the N_2(I) emission lines relate to changes in the glow discharge that directly influence growth conditions. The results show that a poisoned target produces ferroelectric wz-$Al_{0.6}Sc_{0.4}N$ with a reversible 80 μC cm^{-1} polarization and 3.1 MV cm^{-1} coercive

© 2021 The Authors. physica status solidi (RRL) Rapid Research Letters published by Wiley-VCH GmbH

field, whereas the mode flucutations lead to no observable ferroelectric switching in the samples containing rocksalt phase. Monitoring the deposition by GD-OES or DC target bias will help to mitigate rocksalt phase formation and improve process reliability for emerging ferroelectric $Al_{1-x}Sc_xN$ especially when pushing toward higher x.

5. Experimental Section

Thin-film $Al_{0.6}Sc_{0.4}N$ samples were produced via reactive RF magnetron sputtering on (111) textured platinized silicon substrates ($Pt/TiO_2/SiO_2/Si$) with a rocking curve (ω) FWHM $< 1.3°$. The growth chamber had a base pressure of 5×10^{-7} Torr. During the deposition, the pressure was set to 2 mTorr with gas flow rates of 15/5 sccm for Ar/N_2. The substrate temperature was set to 400 °C while rotating at 20 rpm at a distance of 16.5 cm from the target. This relatively low substrate temperature was chosen to avoid spinodal decomposition.[17] A 3″ $Al_{0.6}Sc_{0.4}$ alloy target (Stanford Advanced Materials, 99.9 at% pure) was used with a 6.6 W cm^{-1} forward power density. The target was presputtered for 60 min under the same parameters as the deposition to reduce target surface oxidation.

In situ monitoring consisted of an OES and an RGA. The light emitted from the glow discharge was collected through a 3° collimator lens aimed at the substrate surface by an EPP2000-UVN-SR spectrometer (StellarNet Inc.) with a 0.5 nm resolution (Figure S7, Supporting Information). The fiber optic feedthrough was mounted by a ConFlat (CF) flange flange to the deposition chamber. The relative intensity of the N_2(I) line as a function of time t shown in Figure 3a is a ratio of the $I(t)/I_o$ after subtracting the background signal which was collected prior to striking the glow discharge, where I_o is the initial spectrum collected as a reference. For OES collection, ten spectra were subsequently collected for 5 s each and then averaged, which led to a 50 s time interval between each data point. This was performed to increase the signal to noise because the glow discharge density is much lower near the substrate surface than the target surface.

To investigate the crystal structure, XRD (Bruker D8 Discover) and SAED were used. A 2D detector XRD is used as a faster method for initial screening of sample quality than using a point detector for θ–2θ and ω-rocking curve scans. To produce 1D plots (intensity vs 2θ) from the 2D detector on the Bruker XRD which simultaneously collects intensity in χ and 2θ space during a scan, the intensity is integrated across χ (60–120°). STEM images were acquired using an FEI Talos F200X at 200 keV with a camera length of 77 mm. Cross-sectional lamellae were prepared using an FEI Helios Nanolab 600i FIB/SEM. A cleaning pass was performed at 2 kV to remove Ga implantation and surface damage, and final specimen thicknesses were around 100 nm. Element mapping was performed using EDS, measured in the TEM using a Super-X EDS system. Signal analysis was done using Bruker Esprit 1.9. HR-TEM and resulting FFT analysis was performed using ImageJ for measuring the plane spacings and approximate locations of wurtzite and rocksalt phases in the film.

The films were electrically characterized on parallel plate capacitors with Pt top electrodes deposited through a shadow mask by DC sputtering. Devices were driven from the bottom Pt electrode and sensed from the top Pt contact at an excitation frequency of 10 kHz. The maximum electric field was gradually reduced for each nested loop for determining the coercive field. P–E loops were generated with a Precision Multiferroic system from Radiant Technologies.

Supporting Information

Supporting Information is available from the Wiley Online Library or from the author.

Acknowledgements

This work was co-authored by Colorado School of Mines and the National Renewable Energy Laboratory, operated by the Alliance for Sustainable Energy, LLC, for the U.S. Department of Energy (DOE) under Contract No. DE-AC36-08GO28308. Funding was provided by the DARPA Tunable Ferroelectric Nitrides (TUFEN) program (DARPA-PA-19-04-03) as a part of Development and Exploration of FerroElectric Nitride Semiconductors (DEFENSE) project (diffraction, microscopy, and electrical characterization), and by Office of Science (SC), Office of Basic Energy Sciences (BES) as part of the Early Career Award "Kinetic Synthesis of Metastable Nitrides" (material synthesis and in-situ monitoring). The authors also express their appreciation to Dr. Wanlin Zhu and Prof. Susan Trolier-McKinstry of the Pennsylvania State University for providing $Pt/TiO_2/SiO_2/Si$ substrates. We also thank Dr. Jeff Alleman for assistance with setting up the sputter system at NREL. The data affiliated with this study are available from the corresponding author upon reasonable request. The views expressed in the article do not necessarily represent the views of the DOE or the U.S. Government.

Conflict of Interest

The authors declare no conflict of interest.

Data Availability Statement

The data that support the findings of this study are available from the corresponding author upon reasonable request.

Keywords

aluminum scandium nitrides, ferroelectric films, metallic and poisoned targets, optical emissions, wurtzite

Received: January 19, 2021
Revised: March 10, 2021
Published online: April 24, 2021

[1] R. Wang, X. Liu, I. Shih, Z. Mi *Appl. Phys. Lett.* **2015**, *106*, 261104.
[2] W.-C. Hsu, D.-H. Huang, Y.-S. Lin, Y.-J. Chen, J.-C. Huang, C.-L. Wu, *IEEE Trans. Electron Devices* **2006**, *53*, 406.
[3] M. Akiyama, T. Kamohara, K. Kano, A. Teshigahara, Y. Takeuchi, N. Kawahara, *Adv. Mater.* **2009**, *21*, 593.
[4] K. R. Talley, R. Sherbondy, A. Zakutayev, G. L. Brennecka, *J. Vac. Sci. Technol. A* **2019**, *37*, 060803.
[5] S. Fichtner, N. Wolff, F. Lofink, L. Kienle, B. Wagner *J. Appl. Phys.* **2019**, *125*, 114103.
[6] S. Yasuoka, T. Shimizu, A. Tateyama, M. Uehara, H. Yamada, M. Akiyama, Y. Hiranaga, Y. Cho, H. Funakubo, *J. Appl. Phys.* **2020**, *128*, 114103.
[7] S. Fichtner, T. Reimer, S. Chemnitz, F. Lofink, B. Wagner, *APL Mater.* **2015**, *3*, 116102.
[8] A. Zukauskaite, G. Wingqvist, J. Palisaitis, J. Jensen, P. O.Å. Persson, R. Matloub, P. Muralt, Y. Kim, J. Birch, L. Hultman, *J. Appl. Phys.* **2012**, *111*, 093527.
[9] M. Akiyama, K. Umeda, A. Honda, T. Nagase, *Appl. Phys. Lett.* **2013**, *102*, 021915.
[10] G. Wingqvist, F. Tasnádi, A. Zukauskaite, J. Birch, H. Arwin, L. Hultman, *Appl. Phys. Lett.* **2010**, *97*, 112902.
[11] Y. Lu, M. Reusch, N. Kurz, A. Ding, T. Christoph, M. Prescher, L. Kirste, O. Ambacher, A. Žukauskaitė, *APL Mater.* **2018**, *6*, 076105.

© 2021 The Authors. physica status solidi (RRL) Rapid Research Letters published by Wiley-VCH GmbH

[12] M. Akiyama, K. Kano, A. Teshigahara, *Appl. Phys. Lett.* **2009**, *95*, 162107.
[13] O. Zywitzki, T. Modes, S. Barth, H. Bartzsch, P. Frach, *Surf. Coat. Technol.* **2017**, *309*, 417.
[14] A. Žukauskaitė, C. Tholander, F. Tasnádi, B. Alling, J. Palisaitis, J. Lu, P. O. Å. Persson, L. Hultman, J. Birch, *Acta Mater.* **2015**, *94*, 101.
[15] C. S. Sandu, F. Parsapour, S. Mertin, V. Pashchenko, R. Matloub, T. LaGrange, B. Heinz, P. Muralt, *Phys. Status Solidi A* **2019**, *216*, 1800569.
[16] F. Tasnádi, B. Alling, C. Höglund, G. Wingqvist, J. Birch, L. Hultman, I. A. Abrikosov, *Phys. Rev. Lett.* **2010**, *104*, 137601.
[17] K. R. Talley, S. L. Millican, J. Mangum, S. Siol, C. B. Musgrave, B. Gorman, A. M. Holder, A. Zakutayev, G. L. Brennecka, *Phys. Rev. Mater.* **2018**, *2*, 063802.
[18] S. Mishin, Y. Oshmyansky, *presented at IEEE Int. Ultrason. Symp.*, Kobe, Japan, October 2018.
[19] A. Brudnik, A. Czapla, E. Kusior *Thin Solid Films* **2005**, *478*, 67.
[20] D. L. Ma, H. Y. Liu, Q. Y. Deng, W. M. Yang, K. Silins, N. Huang, Y. X. Leng *Vacuum* **2019**, *160*, 410.
[21] W. Wang, W. Yang, Z. Liu, H. Wang, L. Wen, G. Li *Sci. Rep.* **2015**, *5*, 11480.
[22] S. Tungasmita, J. Birch, L. Hultman, E. Janzén, J.-E. Sundgren *Mater. Sci. Forum* **1998**, *264–268*, 1225.
[23] P. Pigeat, T. Easwarakhanthan *Thin Solid Films* **2008**, *516*, 3957.
[24] S. R. Kirkpatrick, S. L. Rohde, D. M. Mihut, M. L. Kurruppu, J. R. Swanson III, D. Thomson, J. A. Woollam, *Thin Solid Films* **1998**, *332*, 16.
[25] B. Saha, S. Saber, G. V. Naik, A. Boltasseva, E. A. Stach, E. P. Kvam, T. D. Sands *Phys. Status Solidi B* **2015**, *252*, 251.
[26] A. Bousquet, L. Spinelle, J. Cellier, E. Tomasella *Plasma Processes Polym.* **2009**, *6*, S605.
[27] F. Martin, P. Muralt, M.-A. Dubois, A. Pezous *J. Vac. Sci. Technol. A* **2004**, *22*, 361.

© 2021 The Authors. physica status solidi (RRL) Rapid Research Letters published by Wiley-VCH GmbH